Journal of Materials Chemistry A

ROYAL SOCIETY OF CHEMISTRY

PAPER

View Article Online
View Journal | View Issue

Cite this: J. Mater. Chem. A, 2026, 14, 12116

Efficient and selective seawater oxidation by manganese ferrite electrocatalysts obtained *via* a vapor phase strategy

Alessandro Bigiani,[a] Alberto Gasparotto, *[a] Gian Andrea Rizzi, [a] Cinzia Sada,[b] Raffaella Signorini,[a] Alessia Famengo,[c] Davide Barreca, *[d] Oleg I. Lebedev, [e] Evgeny Modin,[f] Mamour Sall [g] and Chiara Maccato [ad]

Electrolysis of seawater is an appealing route for the production of green hydrogen without any stress on drinkable freshwater reservoirs, but its large-scale exploitation is harshly limited by the anodic chlorine oxidation reaction (ClOR), resulting in material corrosion and limiting the efficiency and sustainability of this technology. Consequently, active, stable, and eco-friendly electrocatalysts capable of selectively promoting the oxygen evolution reaction (OER), suppressing thus ClOR, are highly demanded for further advancements in the field. In this context, the present work reports for the first time on the fabrication of crystalline manganese ferrite thin films by an original chemical vapor deposition (CVD) route, starting from a mixture of Mn and Fe β-diketonate diamine adducts acting as single-source precursor for the target systems. Controlled variations of the relative precursor amounts allowed to modulate the structural and compositional characteristics of the resulting materials, with particular regard to the Mn/Fe ratio. Electrochemical tests in real seawater environments yielded, for the best performing system, an outstanding Tafel slope of ≈60 mV dec^{-1}, and enabled to rule out hypochlorite generation. These performances, accompanied by an appreciable operational stability, underscore the potential of the present electrocatalysts for renewable energy-related applications.

Received 17th December 2025
Accepted 16th February 2026

DOI: 10.1039/d5ta10304e

rsc.li/materials-a

1. Introduction

The ever-growing environmental pollution and exponentially raising global energy demand have considerably promoted the exploration of alternative technologies for the production of sustainable energy from largely available natural resources.[1–10] In this regard, electrocatalytic water splitting is a strategically attractive process, especially if powered by renewable energy, to obtain high-purity green hydrogen.[4,11–14] In fact, the large-scale production of H_2 free from any ecological footprint is the cornerstone enabling zero-carbon emissions and providing a promising platform to integrate intermittent renewable energy sources.[5,15,16] Owing to the scarcity of potable water necessary for human life, particularly in arid/hot developing countries, the use of seawater for electrolytic processes to yield hydrogen stands as a powerful avenue in the pursuit of a more sustainable energy infrastructure, satisfying the progressively increasing worldwide needs in a cleaner perspective.[1,17–19] Despite seawater, corresponding to ≈97% of Earth's total H_2O resources, represents an ideal feedstock for H_2 generation alleviating the shortage of freshwater reservoirs,[16,20,21] the concurrence of various critical challenges related to its complex composition still hinders its large-scale exploitation, since clogging/poisoning of catalyst surface, along with the occurrence of undesired side-reactions, result in a lowered process efficiency.[1,19,22] Specifically, a key problem is related to the high salt concentration and, in particular, the presence of Cl^- ions in natural seawater (≈0.5 M), rendering the anodic chlorine oxidation reaction (ClOR) kinetically competitive with the oxygen evolution reaction (OER).[3,19,23–25] The latter, a sluggish four-electron transfer process characterized by an inherently high energy barrier, represents the bottleneck of hydrogen production through water splitting.[11,18,23,26,27] As a matter of fact, under alkaline conditions (pH > 7.5), ClOR maintains the largest thermodynamic potential difference (480 mV) with respect to OER, providing thus a favourable bias window to achieve a good OER selectivity.[1,3,18,26] In fact, if ClOR is not efficiently suppressed, chlorine-containing species can promote

[a]Department of Chemical Sciences, Padova University and INSTM, 35131 Padova, Italy. E-mail: alberto.gasparotto@unipd.it
[b]Department of Physics and Astronomy, Padova University and INSTM, 35131 Padova, Italy
[c]CNR-ICMATE, 35127 Padova, Italy
[d]CNR-ICMATE, INSTM, Department of Chemical Sciences, Padova University, 35131 Padova, Italy. E-mail: davide.barreca@cnr.it
[e]Laboratoire CRISMAT, UMR 6508 Normandie Université, CNRS, ENSICAEN, UNICAEN, 14050 Caen Cedex 4, France
[f]CIC NanoGUNE BRTA, 20018 Donostia, San Sebastian, Spain
[g]CIMAP Normandie Université, CEA, CNRS, ENSICAEN, UNICAEN, 14000 Caen, France

electrocatalyst corrosion/deactivation, resulting in adverse performance and stability deterioration.[16,23,26] At present, the benchmark OER electrocatalysts are based on noble metals (*e.g.* Ru and Ir), but their real-world application is restricted by the high cost, supply shortage, and limited long-term stability, especially in corrosive environments.[5,11–13,16,25,26] As a consequence, remarkable efforts are actually being dedicated to the implementation of stable, economically viable, and eco-friendly electrocatalysts capable of efficiently and selectively sustaining OER in alkaline seawater splitting.[3,4,12,14,16,18,28,29]

In recent years, spinel-type iron-based oxides (AFe_2O_4, where A stands for a first-row transition metal) have emerged as attractive candidates for OER applications,[5,25,30,31] thanks to the green character, versatile compositional/structural features, abundant reaction sites, and low-cost synthesis.[1,8,13,24,32–35] As concerns alkaline seawater electrolysis, such materials have been demonstrated as efficient and corrosion-resistant OER catalysts, paving thus the way to possible large-scale end-uses.[24] Among these systems, $MnFe_2O_4$ has a spinel-type structure, in which oxygen atoms form a face-centered cubic array featuring multiple iron and manganese distributions.[14,36] In particular, whereas Fe sites can readily promote water splitting, Mn ones are mainly responsible for a considerable OER selectivity.[1,5] Nonetheless, in spite of different works devoted to Mn–Fe oxides as electrocatalysts for OER in freshwater splitting,[4–6,8,13,14,25,28–31,37,38] only a few papers have reported on their utilization for OER in seawater,[1,19] highlighting the need of additional fundamental investigation to fully exploit their potential in this field.

On this basis, in this work we focus on the preparation and physicochemical investigation of spinel-type manganese ferrite (MFO) films as anodic electrocatalysts for seawater splitting. Based on our previous studies on Mn[11,39,40] and Fe oxides,[41–43] in the present study we propose as a proof-of-concept, for the first time, a single-step chemical vapor deposition (CVD) route for the lab-scale fabrication of the target systems, based on the simultaneous vaporization of $M(hfa)_2TMEDA$ (M = Mn and Fe; hfa = 1,1,1,5,5,5-hexafluoro-2,4-pentanedionate; TMEDA = *N*,*N*,*N*′,*N*′-tetramethylethylenediamine) molecular sources.[17,44–46] Prior to the deposition process, thermal analyses were carried out on manganese and iron precursors to assess their CVD applicability and the consistency of their vapor pressures for their use as a single-source precursor mixture. Thanks to the very similar volatility of the two compounds, the adopted procedure enabled a direct modulation of the system structural and compositional characteristics by simple changes of the precursor molar ratio (from Mn : Fe = 1 : 2 to Mn : Fe = 2 : 1). Compared to traditional multi-step hydrothermal or solid-state reactions, the developed synthetic strategy offers several advantages including precise control over film composition, optimal uniformity and mechanical adhesion of the obtained deposits, along with process compatibility with different substrates.

Following a thorough physicochemical material characterization by complementary analytical tools, the developed systems were subjected to electrochemical tests to evaluate their functional behaviour as anodes for seawater splitting under alkaline conditions, similar to those adopted in commercial electrolyzers.[23] The obtained results demonstrated that the best electrocatalyst was the Mn : Fe = 1 : 2 system, featuring performances [Tafel slope: ≈60 mV dec^{-1}; current density of 2.87 mA cm^{-2} at 1.80 V *vs.* the reversible hydrogen electrode (RHE)] well placed among those reported for electrocatalysts based on Mn and Fe oxides/hydroxides, as well as for various benchmark RuO_2 and IrO_2 systems. Furthermore, the considerable material stability, demonstrated by prolonged electrochemical tests and post-mortem characterization, open the door to their use in carbon-free sustainable energy production through an advantageous exploitation of the natural capital.

2. Experimental section

2.1 Synthesis

$Mn(hfa)_2TMEDA$ and $Fe(hfa)_2TMEDA$ precursors were synthesized following previously reported procedures.[17,44,45] Thermogravimetric (TGA) and differential scanning calorimetry (DSC) analyses were performed under flowing N_2 (60 mL min^{-1}) at ambient pressure using a Netzsch STA 449 C analyzer (sample weight ≈6–8 mg; heating rate = 10 °C min^{-1}, Al_2O_3 crucibles). Data were processed and analyzed by Netzsch Proteus software.

MFO films were fabricated using a custom-built hot-wall thermal-CVD apparatus consisting of a quartz tube reactor (diameter = 9.5 cm) housed in a Carbolite HST 12/200 tubular furnace.[39] The adopted operating conditions (summarized in Scheme 1) were identified by a series of initial optimization experiments. In each growth process, a ground mixture (overall mass = 0.3 g) of $Mn(hfa)_2TMEDA$ and $Fe(hfa)_2TMEDA$ in a 1 : 2, 1 : 1 or 2 : 1 molar ratio was placed into an external glass vessel heated at 70 °C. The vapors were transported into the reactor by an electronic grade N_2 flow [rate = 100 standard cubic centimetres per minute (sccm)] through gas lines maintained at 120 °C in order to avoid undesired condensation phenomena. An independent electronic grade O_2 flow (rate = 30 sccm) was introduced into the chamber after passing through a water reservoir maintained at 30 °C. Depositions were performed at 400 °C and 3.0 mbar for 2 h on pre-cleaned[41] 1 × 2 cm^2 FTO-coated glass (Aldrich, ≈7 Ω sq^{-1}, FTO thickness = 600 nm), a substrate commonly used for lab-scale fundamental research studies. Finally, the obtained samples were subjected to an *ex situ* thermal treatment at 500 °C for 1 h in a N_2 atmosphere. For comparison purposes, depositions were conducted even from the sole Mn or Fe precursors under the same operating conditions. All the data reported in the present work, except for Fig. S2, are referred to annealed specimens.

2.2 Characterization

X-ray diffraction (XRD) measurements were performed in a glancing incidence mode (ϑ_i = 1.0°) by a Bruker AXS D8 Advance Plus diffractometer equipped with a CuKα X-ray source (λ = 1.54051 Å) powered at 40 kV, 40 mA and a Göbel mirror. The setup used for Raman measurements involved an argon-ion laser (Spectra Physics), operating at λ = 514 nm. The laser was integrated with an Olympus BX 40 microscope, equipped with

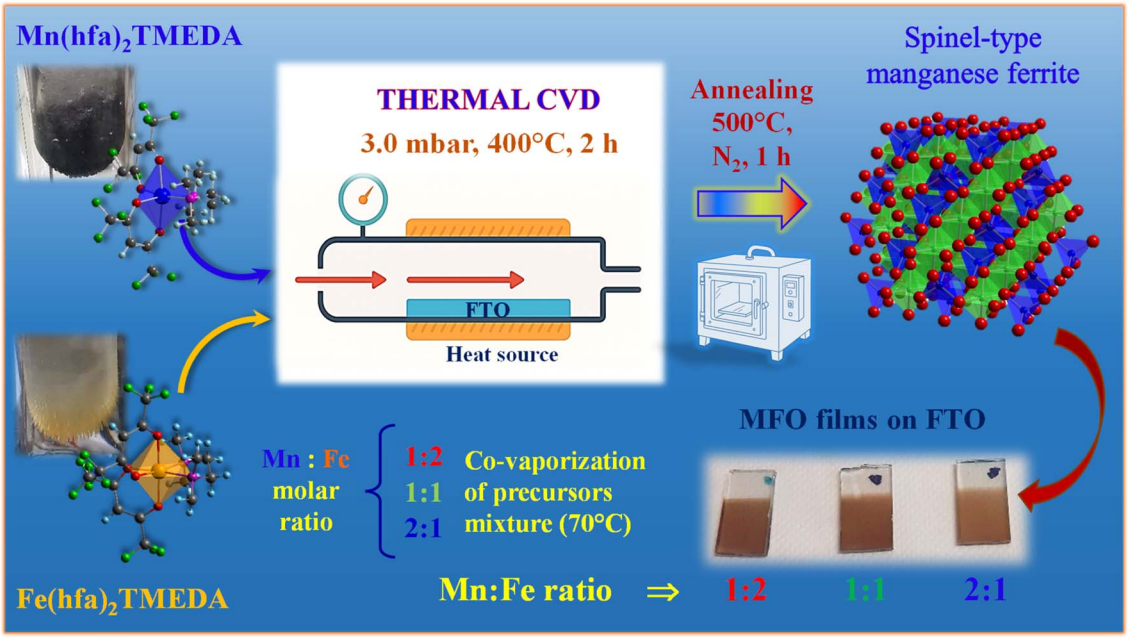

Scheme 1 Sketch of the approach used for the CVD synthesis of MFO electrocatalysts on FTO substrates. The main operating conditions are also reported. Depositions yielded homogeneous and well-adherent films with an orange-brownish colour (photograph in the bottom right corner).

4×, 10×, 20×, 50×, and 100× magnifications objectives (Olympus SLMPL series). The apparatus incorporated edge and notch filters, removing the elastic scattering component from the resulting spectrum and enabling the selection of Raman Stokes transitions. X-ray photoelectron spectroscopy (XPS) and reflection electron energy loss spectroscopy (REELS) measurements were conducted on a Thermo Scientific ESCALAB™ QXi spectrometer, employing a monochromatic Al Kα X-ray source ($h\nu$ = 1486.6 eV). BE values were corrected for charging by referencing to the adventitious C 1s signal at 284.8 eV. Atomic percentages (at%) were estimated by peak area integration using ThermoFisher sensitivity factors. REELS spectra were registered using a primary electron beam energy of 1000 eV. Secondary ion mass spectrometry (SIMS) analyses were carried out by a Cameca IMS 4f mass spectrometer, using a 14.5 keV Cs^+ primary ion beam (current = 30 nA, stability = 0.1%) and by negative secondary ion detection, using an electron gun for charge compensation. Analyses were performed in high mass resolution configuration and beam blanking mode, rastering over a 150 μm × 150 μm area and collecting secondary ions from a 7 μm × 7 μm sub-region to avoid crater effects. The erosion time was converted into depth using thickness values measured by cross-sectional field emission-scanning electron microscopy (FE-SEM). FE-SEM and energy-dispersive X-ray spectroscopy (EDXS) analyses were carried out using a Zeiss SUPRA 40VP instrument equipped with an INCA x-act PentaFET Precision spectrometer, at primary beam voltages between 10 and 20 kV. The average deposit thickness values and particle dimensions were evaluated through a statistical image analysis using the ImageJ® software,[47] averaging over 20 independent measurements in each case. Atomic force microscopy (AFM) was performed using a NT-MDT SPM Solver P47H-PRO instrumentation operated in air and in tapping mode. Transmission electron microscopy (TEM) analysis, including bright field high resolution TEM (BF-HRTEM), high-angle annular dark-field scanning TEM (HAADF-STEM), EDXS elemental mapping in STEM mode and electron diffraction (ED), was carried out by means of a double-aberration corrected cold FEG JEM ARM200F microscope operating at 200 kV and equipped with a large angle CENTURIO EDX detector, an ORIUS Gatan camera and a Quantum GIF. Electron energy loss spectroscopy (EELS) experiments were performed in dual-EELS mode for elemental analysis using a Gatan K3 detector with a collection angle of 30 mrad, a beam convergence angle of 15 mrad, and an energy dispersion of 0.9 eV per channel. To further investigate the Fe and Mn local chemical environment, EELS measurements were also carried out with a lower dispersion energy (0.03 eV per channel). STEM micrographs and EELS data were acquired and processed under the Gatan Digital Micrograph.

Electrochemical functional tests were carried out by means of an integrated system consisting of a Zennium-PRO and a PP212 unit from Zahner GmbH, coupled with an optical bench containing a test cell,[26] using a MMO (Hg/HgO) reference electrode, a Pt coil as counter-electrode, and FTO-supported systems as working electrodes. Linear sweep voltammetry (LSV; scan rate = 5 mV s^{-1}) measurements were first carried out in simulated alkaline seawater (0.5 M KOH + 0.5 M NaCl),[23,48] and subsequently in Adriatic seawater picked up at Rosolina (RO), Italy. Real seawater was pre-treated adding KOH and separating the resulting precipitate [mainly formed by $Mg(OH)_2$; final pH = 13.6],[23] along with other suspended solids, by filtration. This is a low-cost and simple procedure, ensuring a better reproducibility of lab-scale results, avoiding complications due to solid impurities, and hindering the oxidation of Cl^-

ions.[49] Tafel slopes were obtained by plotting the overpotential *vs.* RHE against log(current density).[1,4,13,14,28]

Chronoamperometry (CA) analyses were performed at a fixed potential of 1.80 V *vs.* RHE.[29] The possible presence of hypochlorite species was assessed by iodometric titration experiments. Further details on material physicochemical and functional characterization are reported in the SI.

3. Results and discussion

3.1 Material characterization

The fabrication strategy proposed in the present work for the CVD synthesis of MFO films involved the vaporization of 1 : 2, 1 : 1 or 2 : 1 molar mixtures of $Mn(hfa)_2TMEDA$ and $Fe(hfa)_2$-TMEDA precursors. The ultimate aim was the obtainment of ternary spinel phase materials by the reaction of the two precursors on the growth surface, with a direct control over the Mn/Fe ratio in the resulting deposits. To fully benefit from such advantages, the co-vaporized precursors must be endowed with very similar thermal behaviors, and, accordingly, preliminary TGA analyses were undertaken. As can be observed in Fig. 1a, for both the precursors and their mixture, a single-step weight loss occurred at temperatures higher than ≈100 °C, yielding a residual mass close to zero for $T > 190 \div 200$ °C. These results are the finger-print of a quantitative vaporization free from any premature side-decomposition for both the pure precursors and their mixture. DSC analyses (Fig. S1) enabled to identify two endothermic peaks at 77–85 °C and 186–194 °C, corresponding to melting and subsequent vaporization, respectively,[17,44,45] whereas no other signals were detected at higher temperatures. The Arrhenius plots in Fig. 1b reveal very close vaporization rates of the two precursors throughout the investigated temperature range. The apparent molar vaporization enthalpy (ΔH_{vap}) could be evaluated by the slope of experimental curves, yielding $\Delta H_{vap} = (71 \pm 1)$ kJ × mol^{-1} and (69 ± 1) kJ × mol^{-1} for $Mn(hfa)_2TMEDA$ and $Fe(hfa)_2TMEDA$, respectively. Taken together, these results underscore a very similar thermal behaviour of the two precursors, of key importance for their consistent co-vaporization in CVD processes to achieve a controlled and reproducible growth of MFO films.

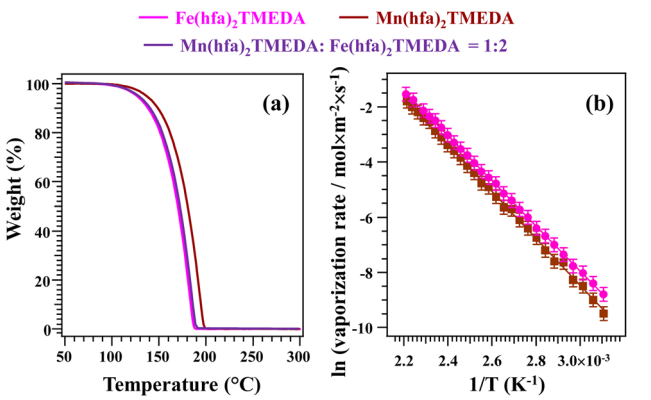

Fig. 1 (a) TGA curves in N_2 for $Mn(hfa)_2TMEDA$ (brown), $Fe(hfa)_2$-TMEDA (pink) and their 1 : 2 mixture (violet). (b) Arrhenius plots for the vaporization of the two precursors (temperature interval ≈50 ÷ 180 °C).

XRD patterns and Raman spectra for the obtained materials are reported in Fig. 2a and b, respectively. In the former case, beside FTO substrate signals, relatively weak peaks at ≈18.1, 29.6, 35.0, 36.5 and 56.1° were detected and assigned to the (111), (220), (311), (222) and (511) reflections of a MFO cubic spinel phase ($Fd\bar{3}m$ space group, *jacobsite*).[50,51] This attribution was further supported by Raman results (Fig. 2b), revealing two main bands pertaining to manganese ferrite films. In general, five Raman active modes are predicted for cubic spinels by factor group analysis, *i.e.* $A_{1g} + E_g + 3T_{2g}$.[52,53] In this regard, the band located in the 600–660 cm^{-1} wavenumber range is assigned to symmetric stretching of M–O bonds (M = Mn or Fe) in tetrahedral sites (A_{1g} mode), whereas the band at 430–470 cm^{-1} is related to the typical T_{2g} vibrations from octahedral ones.[52–55] As can be observed, both peaks underwent a red-shift (≈15 cm^{-1}) on going from the Mn : Fe = 1 : 2 specimen to the Mn : Fe = 2 : 1 one. It is well known that the frequencies of Raman modes depend on the effective mass and force constant of vibrating species at tetrahedral and octahedral sites that, in turn, are affected by the nature and oxidation state of the involved metal centers.[52,55,56] Therefore, the occurring peak shift suggests that more than one type of cation (principally Fe^{3+} and Mn^{2+}, see XPS and EELS results below) occupies both tetrahedral and octahedral sites, whose population is also directly affected by the Mn : Fe ratio in the corresponding specimens.[52] Interestingly, XRD and Raman spectra very similar to Fig. 2 ones were obtained for the corresponding as-prepared samples (see Fig. S2a and b). This result suggested that the formation of the ternary spinel phase took place already during the CVD process and was not directly induced by annealing, whose main effect was a moderate increase in the system crystallinity. On the other hand, the separate vaporization of Mn and Fe precursors yielded, respectively, the formation of the tetragonal α-Mn_3O_4 (ref. 57) and rhombohedral α-Fe_2O_3 (ref. 58) phases, whose occurrence was preserved even after thermal treatment (Fig. S2c and d). Altogether, these findings highlight that co-vaporization of the two precursors affects their intrinsic reactivity and favours the obtainment of a cubic manganese ferrite spinel phase.

Information on surface composition was gained by XPS. In all cases, wide-scan spectra (Fig. S3) featured the main photoelectron and Auger signals of Mn, Fe, O, and C (see also Fig. S4a). Quantitative analyses (Table S1 and Fig. 3a) indicated that the Mn/Fe at% ratio values in the obtained deposits were very close to the nominal composition expected based on the mixing ratio of the two precursors, validating thus a "direct transfer" of Mn/Fe ratio from the precursor source to the target samples. This result confirms that $Mn(hfa)_2TMEDA$ and $Fe(hfa)_2TMEDA$ possess not only a similar vaporization behavior, but also comparable decomposition rates, highlighting the present CVD approach as a reliable route for the compositional control of ternary metal oxides. The $Mn2p_{3/2}$ component was centered at 641.3–641.5 eV [spin orbit separation (SOS) ≈11.7 eV, Fig. 3b]. Such features, along with the presence of shake-up satellites at energies higher than the main components, supported the predominance of Mn^{2+} in the

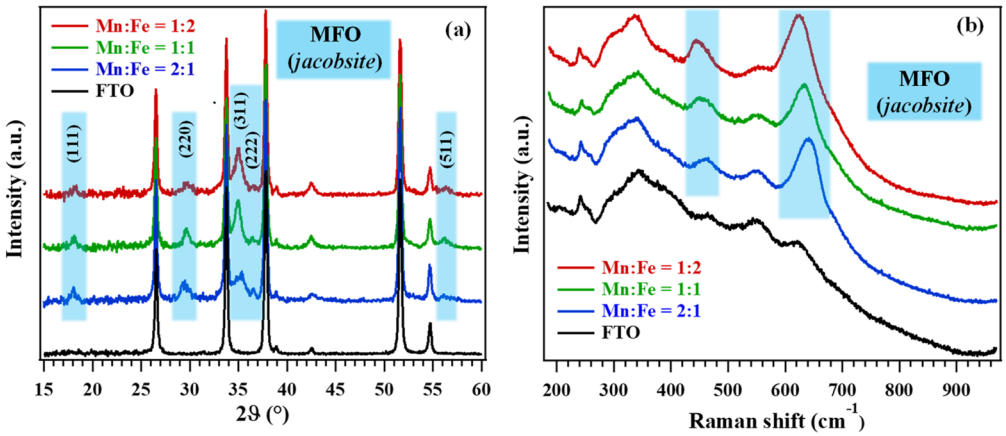

Fig. 2 (a) XRD patterns and (b) Raman spectra for MFO specimens grown on FTO from different mixtures of $Mn(hfa)_2TMEDA$ and $Fe(hfa)_2TMEDA$ precursors. Curves have been vertically shifted for clarity. The XRD pattern and Raman spectrum of the bare FTO substrate are also reported for comparison. In both panels, the main signals from the MFO spinel phase are highlighted by a pale blue background.

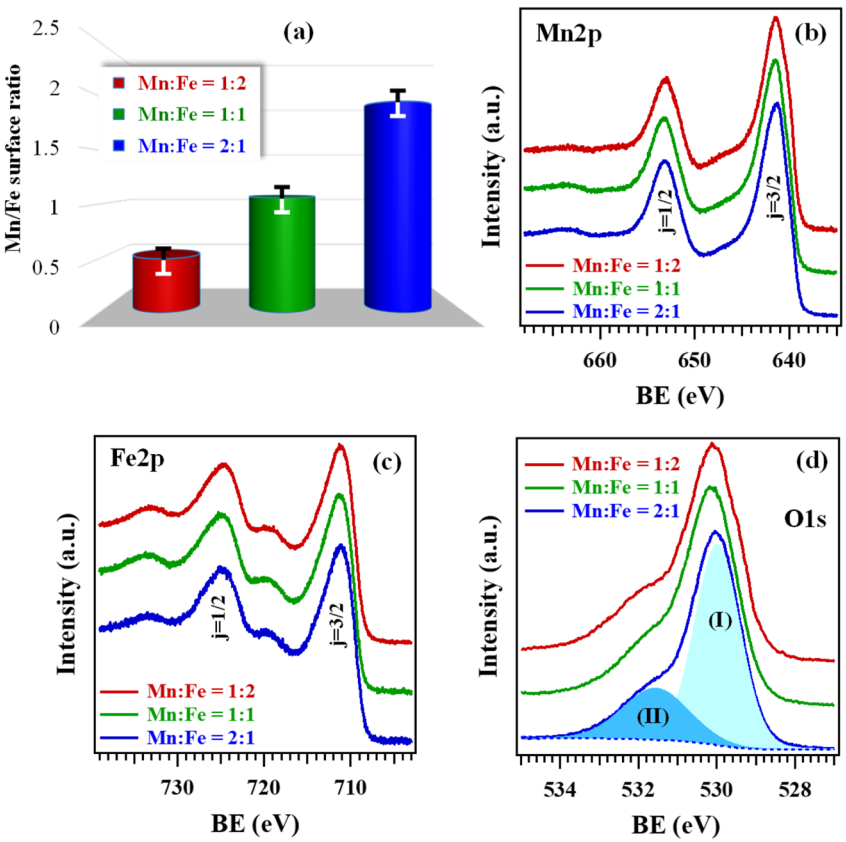

Fig. 3 (a) Mn/Fe surface at% ratio, obtained from XPS analyses, *vs.* the molar ratio of the starting precursor mixture. Mn 2p (b), Fe 2p (c), and O 1s (d) photopeaks for MFO electrocatalysts obtained from different mixtures of Mn and Fe precursors.

analyzed materials.[7,32,34,59] However, a careful analysis of Fig. 3b evidenced a slight Mn 2p blue shift upon going from the Mn : Fe = 1 : 2 sample to the Mn : Fe = 2 : 1 one. This effect, along with the parallel intensity reduction of shake-up satellites, suggested the presence of some Mn^{3+} centers in the more Mn-rich samples.[60,61] In this regard, valuable insights were obtained by the Mn 3s multiplet splitting separation (MSS; Fig. S4b), a useful fingerprint for manganese valence state.[62,63] Data analysis yielded the following MSS values of 6.1, 5.9, and 5.8 eV for Mn : Fe = 1 : 2, 1 : 1, and 2 : 1, respectively. The corresponding Mn average oxidation state can be estimated as +2.0, +2.1, and +2.3.[21,63] Interestingly, the same conclusion was supported even by the BE difference between the Mn $2p_{3/2}$ signal and the O 1s lattice oxygen component (111.2, 111.3, and

111.5 eV for Mn : Fe = 1 : 2, 1 : 1, and 2 : 1, respectively)[64] and by EELS results (see below). The Fe $2p_{3/2}$ band (Fig. 3c) was centered at ≈711.0–711.3 eV, and showed a separation of ≈13.7 eV from the Fe $2p_{1/2}$ one. These values, together with the shake-up satellites located at BEs ≈8 eV higher than the main spin–orbit components, demonstrated the net predominance of Fe^{3+} in all samples, and were consistent with results reported for manganese ferrite spinels.[7,28,32,35,59,65] Nonetheless, its energy position downshifted from 711.3 eV (Mn : Fe = 1 : 2), to 711.2 eV (Mn : Fe = 1 : 1), and finally to 711.0 eV (Mn : Fe = 2 : 1), a result suggesting the possible presence of minor Fe^{2+} amounts for higher Mn content.[60,66] For all samples, the O 1s peaks (Fig. 3d) was deconvoluted by a main component at 530.1 eV (≈70% of the overall area), due to lattice O,[23,40,60] and a second one at 531.7 eV, ascribed to –OH groups chemisorbed on O vacancies.[23,40,46,60] Oxidized C-containing species also contributed to the latter band (see Fig. S4 and related comments).

Insights into material in-depth composition were provided by SIMS analyses (Fig. 4). Regardless of the analyzed specimen, manganese and iron ionic yields revealed a parallel in-depth profile from the surface down to film/substrate interface, indicating a common chemical origin for the two metals and their even distribution along the whole thickness. Nevertheless, a comparison of Mn and Fe curves between the target samples suggested a progressive increase in the overall Mn : Fe ratio upon going from Fig. 4a–c. These findings, in conjunction with XPS outcomes, corroborated the successful formation of spinel-phase deposits with a uniform in-depth composition and a Mn/Fe ratio tunable as a function of preparative conditions.

Fig. 5a plots both the valence band (VB) region and the secondary electron photoemission cutoff for a Mn : Fe = 1 : 2 sample. Analogous measurements carried out even for the Mn : Fe = 1 : 1 and 2 : 1 systems enabled the estimation of work function (W_F) values (Table S2, SI). REELS spectra (Fig. 5b) allowed to evaluate material band gaps (Table S2, SI), and, altogether, to construct the band scheme proposed in Fig. 5c. All the specimens featured W_F values in the range 3.6–4.1 eV.[67,68] E_G values (that were found to slightly decrease from 1.7 eV to 1.4 eV upon varying the Mn : Fe ratio from 1 : 2 to 2 : 1) agreed to a good extent with previous results.[9,54,69,70] The separation of VB edges from the Fermi energy (Fig. 5c and Table S2), in agreement with former works,[54] is in line with the *n*-type material character.[71] Notably, the deeper E_F for the Mn : Fe = 1 : 2 specimen aligns with its superior OER performances.[11,26]

The target materials were further investigated by FE-SEM, EDXS, and AFM (Fig. 6 and S5). For all deposits, FE-SEM micrographs (Fig. 6a–c) revealed a uniform conformal coverage of the underlying substrate. The target MFO materials exhibited relatively large particles (dimensions = 150 ÷ 230 nm), that displayed a more pronounced globular nature as Fe content increased, whereas the sample with the highest Mn loading showed smoother and more compact features. For all the target electrocatalysts, AFM measurements (Fig. 6d–f) yielded root-mean-square roughness (RMS) values very close to 17 nm, suggesting thus a comparable active area.

A deeper insight into the system nanoscale structure was obtained by TEM and related analyses, performed on the specimens with Mn : Fe = 1 : 2 and 2 : 1 ratios (Fig. 7 and 8). In tune with FE-SEM outcomes, low magnification cross-sectional TEM images highlighted the formation of uniform systems (Fig. 7a–c and 8a–b), with a homogeneous distribution of all elements throughout the deposit thickness (Fig. 7d and 8c). In both cases, MFO films followed the faceted surface and zig-zag morphology of the underlying FTO substrates, but their nanostructure was directly dependent on the synthesis conditions. The specimen obtained from a Mn : Fe = 1 : 2 precursor mixture featured nanoaggregates with typical dimensions between 20 and 50 nm (Fig. 7c), while the homologous Mn : Fe = 2 : 1 one showed larger grains. Analyses of ED patterns revealed in both cases a cubic ($Fd\bar{3}m$) structure, in agreement with XRD data. Nonetheless, on account of EDXS quantitative analyses (yielding Mn : Fe atomic ratios of 1 : 2 and 2 : 1, in accordance with XPS, see above) and EELS (Fig. 9), two cubic structures, corresponding to $MnFe_2O_4$ (ref. 72) and Mn_2FeO_4,[73] were proposed. Fig. 7e shows high resolution HAADF-STEM image and Fourier transform (FT) pattern of a selected [101] oriented nanoparticle, which are well fitting with the cubic $MnFe_2O_4$ structure.[72] For a MFO specimen obtained from a Mn : Fe = 2 : 1 precursor

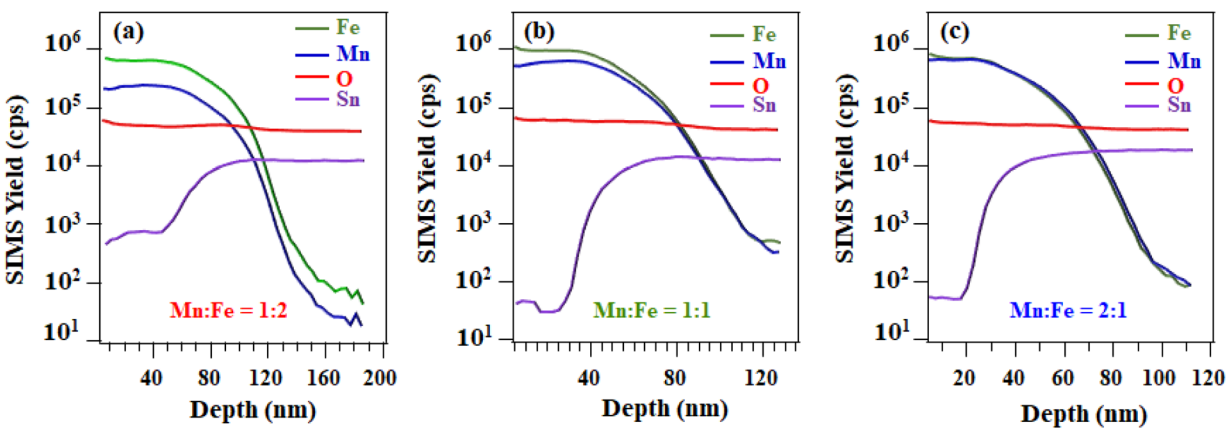

Fig. 4 SIMS depth profiles for MFO films obtained from different Mn and Fe precursors mixtures: (a) Mn : Fe = 1 : 2; (b) Mn : Fe = 1 : 1; (c) Mn : Fe = 2 : 1.

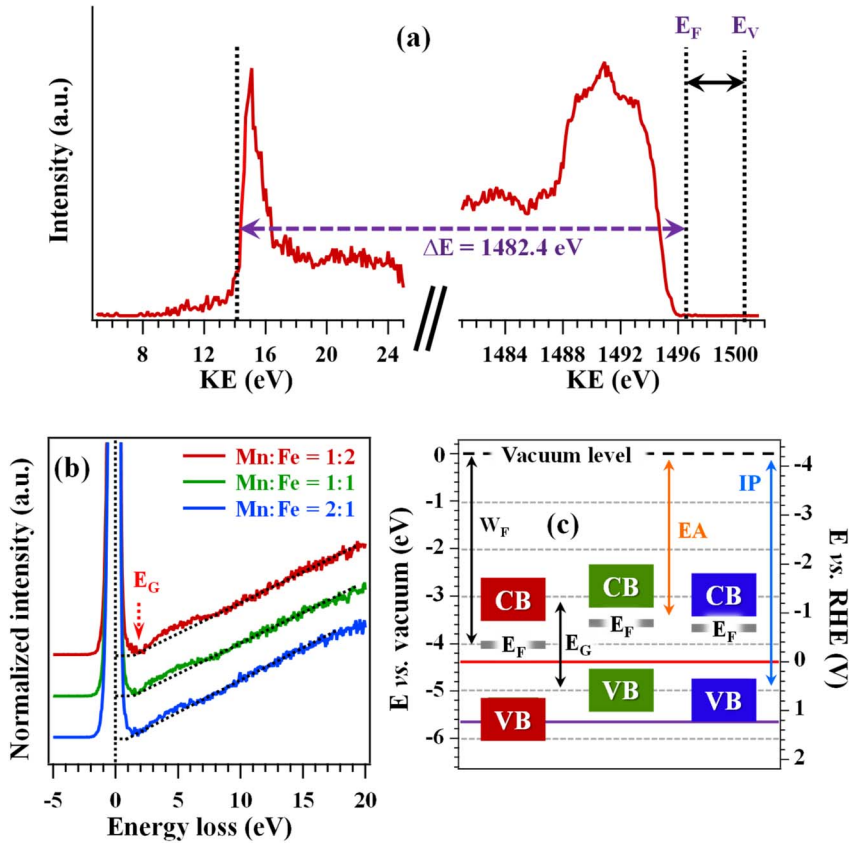

Fig. 5 (a) XPS valence band with photoemission cutoff for a MFO specimen obtained from a Mn : Fe = 1 : 2 precursor mixture. (b) REELS spectra of various electrocatalysts, and (c) corresponding band scheme (KE = kinetic energy; E_F = Fermi energy; E_V = vacuum level; E_G = band gap; CB and VB = conduction and valence band; W_F = work function; EA = electron affinity; IP = ionization potential). Color codes as in panel (b). The horizontal red and violet lines mark the standard potentials of the H^+/H_2 and O_2/H_2O redox couples, respectively.

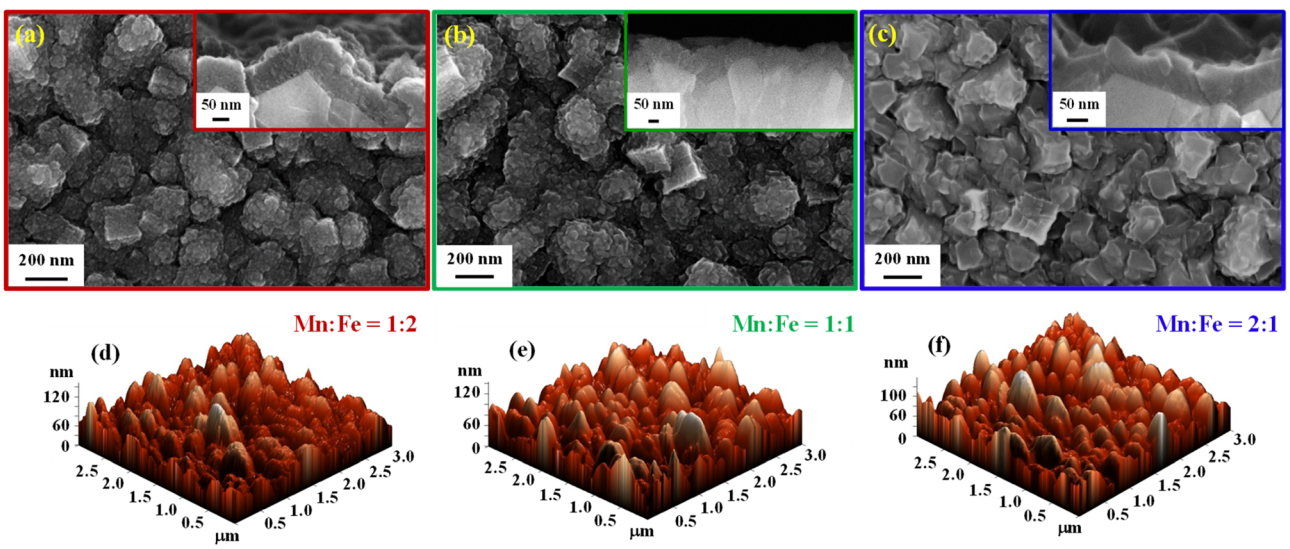

Fig. 6 Plane-view FE-SEM (a–c) and AFM (d–f) micrographs for MFO samples synthesized from different Mn and Fe precursors mixtures: (a and d) Mn : Fe = 1 : 2; (b and e) Mn : Fe = 1 : 1; (c and f) Mn : Fe = 2 : 1. Cross-sectional FE-SEM images are reported as insets in the upper panel.

mixture, HRTEM images and FT patterns of two [111] and [112] oriented grains (Fig. 8d and e) show good correspondence with the cubic $Fd\bar{3}m$ Mn_2FeO_4 structure.[73]

Quantitative EELS analyses were carried out on both specimens featuring Mn : Fe = 1 : 2 and 2 : 1 ratios. As a representative case, Fig. 9a–f display elemental chemical maps for the

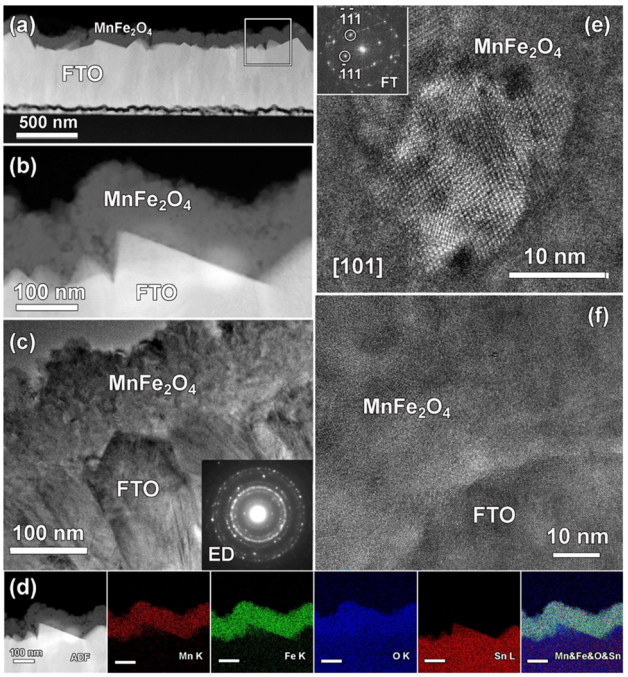

Fig. 7 (a) Cross-sectional low magnification HAADF-STEM image of a sample obtained from a Mn : Fe = 1 : 2 precursor mixture. (b) Magnified image of the region framed by the white box in (a). (c) BF-TEM image of $MnFe_2O_4$/FTO interface and corresponding ring ED pattern. (d) HAADF-STEM image and simultaneously acquired EDXS elemental maps for Mn K, Fe K, O K, and Sn L signals, together with an overlaid color image. (e) High resolution HAADF-STEM image of an individual $MnFe_2O_4$ nanoparticle recorded along the [101] zone axis, and corresponding FT pattern. (f) High resolution HAADF-STEM image of $MnFe_2O_4$/FTO interface.

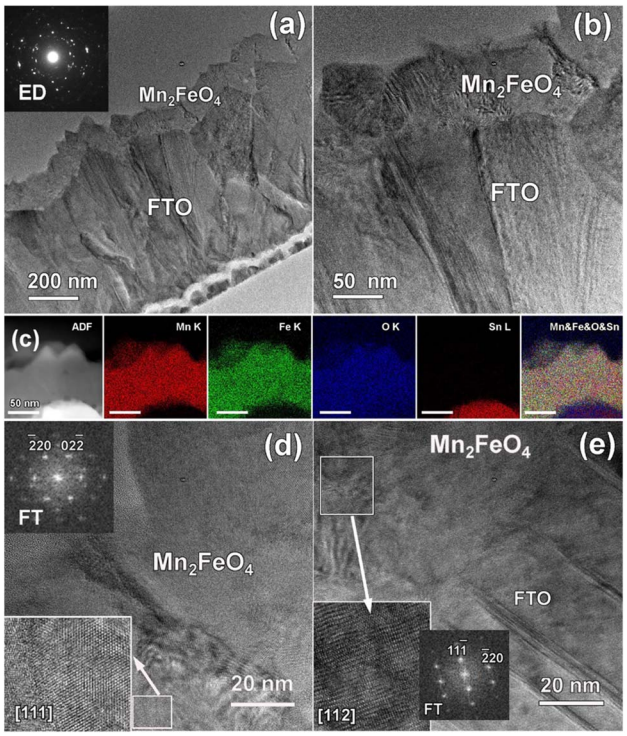

Fig. 8 (a) Cross-sectional low magnification BF-TEM image of a MFO specimen obtained from a Mn : Fe = 2 : 1 precursor mixture and corresponding ED pattern. (b) Magnified BF-TEM image of Mn_2FeO_4/FTO interface. (c) HAADF-STEM image and simultaneously acquired EDXS elemental maps for Mn K, Fe K, O K, Sn L, along with an overlaid color image. (d and e) HRTEM images of Mn_2FeO_4 grains recorded for two main zone axes, *i.e.* [111] and [112], respectively. The magnified areas framed by white boxes and corresponding FT patterns are given as insets.

Mn : Fe = 1 : 2 sample. The chemical composition was determined to be close to $MnFe_2O_4$ and Mn_2FeO_4 for the Mn : Fe = 1 : 2 and Mn : Fe = 2 : 1 specimens, respectively. For a deeper investigation, the valence states of Mn and Fe were studied by measuring their fine structure, characterized by two white-line peaks (L_2 and L_3) whose shape, position and amplitude ratio are directly dependent on the element oxidation state.[74,75] As can be observed in Fig. 9g, the manganese L_3/L_2 amplitude ratio was much lower in the Mn : Fe = 2 : 1 sample (L_3/L_2 = 2.3), indicating a higher Mn^{3+} contribution, differently from the Mn : Fe = 1 : 2 specimen (L_3/L_2 = 3.2), for which Mn^{2+} was largely predominant. In a different way, Fe EELS fine structures (Fig. 9h) were rather similar for both specimens, suggesting that Fe^{3+} centers had an analogous content in both materials, and only minor differences in the Fe^{2+} contribution occurred. It is worthwhile noticing that both the atomic composition and oxidation states of both Mn and Fe are spatially uniform throughout the deposit thickness.

3.2 Electrochemical functional tests

OER electrocatalytic performances of the fabricated materials were first investigated in simulated alkaline seawater (0.5 M KOH + 0.5 M NaCl). LSV traces (Fig. 10a) showed that bare Mn_3O_4 and Fe_2O_3 yielded lower current densities than all the investigated MFO systems, whose performances underwent a systematic enhancement, throughout the whole potential range, according to the sequence Mn : Fe = 2 : 1 < Mn : Fe = 1 : 1 < Mn : Fe = 1 : 2 (Fig. 10b). This conclusion was also supported by the evaluated overpotentials (Fig. 10c), the lowest one being obtained for the Mn : Fe = 1 : 2 electrocatalyst. In agreement with these findings, the Tafel slope, an additional valuable parameter for exploring OER reaction kinetics,[1,6,13,19,25,61] underwent a progressive decrease from the Mn : Fe = 2 : 1 to the Mn : Fe = 1 : 2 electrode (Fig. 10d). The best performing Mn : Fe = 1 : 2 electrocatalyst exhibited the lowest Tafel slope, a result reflecting a higher exchange current density and confirming its better OER performances.[14] Furthermore, a lower slope also relates to a minor energy amount required to drive the reaction at higher rates, a favorable issue for energy-efficient electrochemical processes.[6] In tune with these observations, the same specimen featured also the highest turnover frequency (TOF) (Fig. 10e). The pertaining electrocatalytic performances (Table S3) are well positioned, or even superior, with respect to those exhibited in saline/seawater splitting under alkaline conditions by several single- and mixed-phase systems based on oxides and hydroxides, even functionalized with cobalt(II) phosphate (CoPi), a well-known oxidation co-catalyst (Table S4).[26] In particular, as concerns studies performed in simulated alkaline

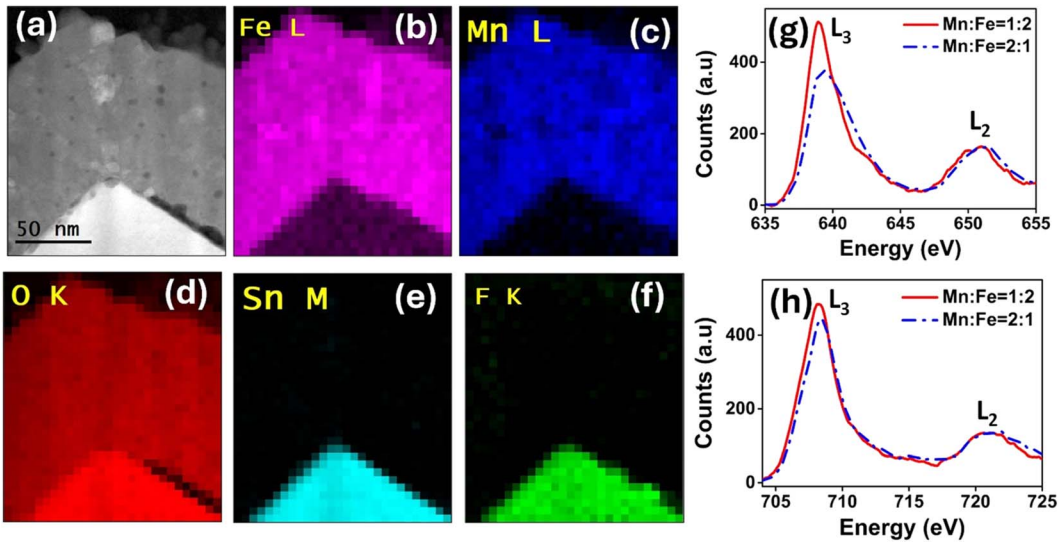

Fig. 9 (a–f) EELS chemical maps of the different elements in the Mn : Fe = 1 : 2 sample. (g) and (h) Comparison of normalized EELS fine structures in the Mn : Fe = 1 : 2 and Mn : Fe = 2 : 1 samples for Mn and Fe, respectively.

seawater, the present systems offer lower Tafel slopes than Mn_2NiO_4,[22] $Ni_{0.85}Fe_{0.15}O$,[12] and both γ- and δ-MnO_2 polymorphs,[16] the latter featuring also a lower OER selectivity.

The potential of the present results is also highlighted by the favorable comparison of material activity with that of different benchmark IrO_2 and RuO_2 electrocatalysts in the splitting of both simulated and real seawater (Table S4). CA traces (Fig. 10a, inset) evidenced that, after an initial current density decrease likely related to the evolution of O_2 bubbles which did not abandon material surface immediately upon gas generation,[76] all the fabricated electrocatalysts featured a very good stability upon prolonged operation. A similar result, corroborated even by the negligible variations displayed by LSV traces upon repeated testing (Fig. S6), is an important pre-requisite in view of an eventual real-world utilization.[25] In a different way, Mn_3O_4 and Fe_2O_3 presented an apparently lower stability (Fig. S7).

To further validate the practical OER feasibility from the used reaction media, additional efforts were dedicated to assessing the catalyst selectivity. Fig. 10f compares the O_2 amount generated throughout 1 h of CA tests at 1.80 V *vs.* RHE with the corresponding theoretical one for the Mn : Fe = 1 : 2 specimen. The obtained results enabled to estimate a Faradaic efficiency of 98%, evidencing a remarkable selectivity towards O_2 generation, a key issue for a practical end-use. In this regard, a favorable effect stems from the presence of oxygen deficiencies in the catalyst structure[1] (whose occurrence is demonstrated by XPS, see above). In fact, these deficiencies, besides favoring an improved charge transfer and a higher conductivity, can generate a higher number of active sites, and decrease the adsorption energy for H_2O molecules. Hence, the appreciable amount of chemisorbed –OH groups (see Fig. 3d and pertaining comments) positively affects the ultimate performances by promoting the generation of a higher O_2 amount.[25]

Based on the attractive results yielded by electrochemical tests in simulated seawater, material OER performances were subsequently assessed in Adriatic alkaline seawater. As shown by LSV traces and Tafel plots (Fig. 11a and b), Mn_3O_4 and Fe_2O_3 yielded again worse performances than MFO systems. The activity trend observed in simulated seawater was maintained, though current density values and the main performance indicators were lower than in the previous case (see also Fig. S8–S9 and Table S3). This result was traced back both to the presence of impurities, the more corrosive environment, and the higher ionic strength of real seawater with respect to its simulated homologous, that, altogether, are responsible for an inferior O_2 yield.[23]

In real alkaline seawater under conditions very similar to the present work, the actual MFO performances are comparable, or even better, than MnO_2 and Mn_2O_3 composites with Co_3O_4 and Fe_2O_3 in terms of Tafel slopes, and offer a higher stability.[23] They also feature an improved OER kinetics than $NiFe_2O_4$ (ref. 77) and the homologous $MnFe_2O_4$, for which the introduction of an external Co shell was necessary to achieve an improved selectivity and to protect the material from dissolution.[19] Importantly, iodometric titration experiments (see Section S1.2) enabled to rule out the formation of any hypochlorite trace, as indicated by the almost colourless OER solution against the pink-colored reference one (Fig. 11c).[1,26] This result, in conjunction with the measurement of O_2 produced during OER (Fig. 11d; Faradaic efficiency = 96%) validated the selectivity towards OER even in real seawater. In a different way, for bare Mn_3O_4 and Fe_2O_3 the formation of corrosive ClO^- was not negligible (Fig. S10), accounting thus for their inferior performances and lower stability in comparison to MFO systems.

A further remarkable benefit for a possible real-world utilization of MFO systems is their stability upon prolonged tests in seawater, as demonstrated by the limited current density losses upon extended utilization, up to 50 h, and repeated testing (Fig. S11 and S12), at variance with bare Mn_3O_4 and Fe_2O_3 (Fig. S13). MFO electrocatalyst stability was further supported by post-*operando* XRD, FE-SEM, and XPS analyses (Fig. S14–

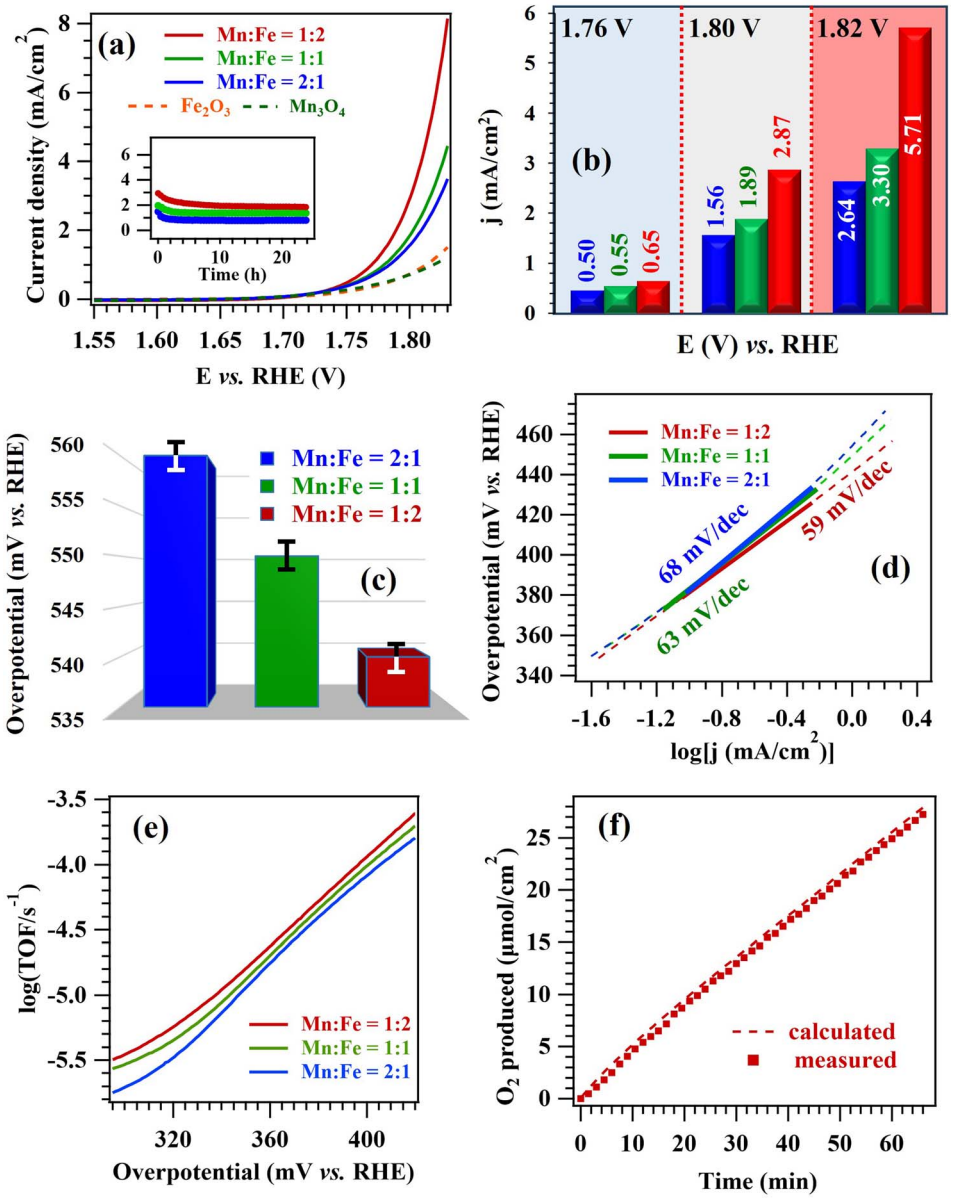

Fig. 10 Electrochemical OER performances of MFO systems in simulated alkaline seawater. (a) *iR*-corrected LSV traces. Mn_3O_4 and Fe_2O_3 curves are also reported for comparison. Inset: chronoamperometric tests for MFO electrocatalysts, performed at 1.80 V *vs.* RHE. (b) Current densities at different bias values. (c) Overpotentials at 1 mA cm^{-2}. (d) Tafel plots; dashed and continuous lines correspond to experimental and fitting curves, respectively. (e) TOF curves *vs.* overpotential for the target electrocatalysts. (f) O_2 evolution *vs.* time for the Mn : Fe = 1 : 2 specimen. The dashed curve was calculated assuming a 100% Faradaic efficiency.

S16), ruling out the occurrence of appreciable structural/morphological degradation and metal leaching in comparison to the pristine materials. The only noticeable effect revealed by XPS survey spectra collected on MFO films after electrochemical tests in real seawater (Fig. S16a) was the presence of Ca^{2+} on the catalyst surface, whereas no significant contributions from other impurities such as Mg^{2+} or Cl^{-} could be appreciated. Hence, the lower electrochemical performances in real seawater compared to simulated one might be due to the adsorption/precipitation of Ca^{2+} species.

Taken together, functional results discussed so far clearly indicate that, regardless of the reaction medium (simulated *vs.* real seawater), the control of Mn/Fe ratio in the obtained materials is of considerable importance to tailor the corresponding OER activity.[28] The important question that now arises is: why do materials with Mn : Fe = 1 : 2 ratio offer a higher activity than those featuring Mn : Fe = 1 : 1 and Mn : Fe = 2 : 1 ratios? Basing on AFM outcomes, that provided very similar RMS roughness values (see above), significant contributions from the system surface area can be ruled out. Indeed, the observed behaviour can be related to the concomitant contribution of different concurring effects. A first one is the deeper Fermi level for the Mn : Fe = 1 : 2 specimen, as already mentioned (see above and Fig. 5c). An additional issue relates to

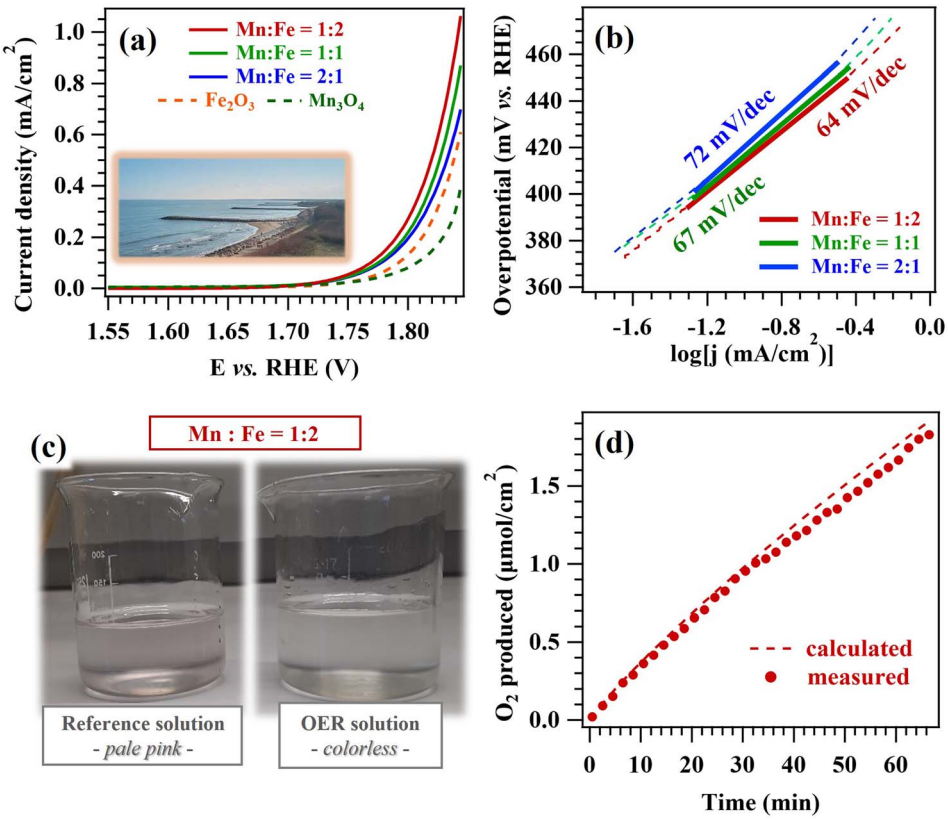

Fig. 11 OER performances of MFO electrocatalysts in Adriatic alkaline seawater, collected at Rosolina seaside (RO), Italy [photograph shown as inset in (a)]. (a) LSV curves. Mn_3O_4 and Fe_2O_3 traces are also displayed for comparison. (b) Tafel plots. Dashed and continuous lines correspond to experimental and fitting curves, respectively. (c) Photographs of the OER and reference solutions taken upon iodometric titration (sample Mn : Fe = 1 : 2), evidencing no ClO^- formation in the latter case. (d) O_2 evolution *vs.* time for the Mn : Fe = 1 : 2 electrocatalyst. The dashed curve was calculated assuming a 100% Faradaic efficiency.

the fastest charge transfer efficiency,[1,25] as demonstrated by electrochemical impedance spectroscopy (EIS) analyses. In fact, in line with previous results,[7,8] charge transfer resistances (R_{CT}) progressively decreased according to the order Mn : Fe = 2 : 1 > Mn : Fe = 1 : 1 > Mn : Fe = 1 : 2 in both simulated and real seawater (compare Fig. S17 and Tables S5–S6). As a matter of fact, a reduced resistance indicates a more efficient charge transport,[6] suggesting a more favourable hole injection efficiency for the Mn : Fe = 1 : 2 material, and correlating with the observed enhancement in OER performances.[14] This behaviour is consistent with literature works reporting on electron hopping processes between mixed-valence (+2/+3) metal cations in spinel ferrites, where octahedrally coordinated metal centres are often associated with higher OER activity.[25,28] In fact, previous studies have suggested that octahedral Fe sites may facilitate water activation, whereas Mn-based oxides exhibit enhanced OER selectivity in seawater splitting, an issue that could be potentially related to a weaker interaction with Cl^- ions.[1,5] More generally, the coexistence of Fe^{3+} and Mn^{2+} species has been proposed to promote favorable redox processes between the two metal centers, which might contribute to improved OER kinetics *via* reduced electron-transfer barriers.[25] These considerations are consistent with the experimental outcomes of the present work. In a different way, for the Mn : Fe = 2 : 1 system, characterized by a higher relative abundance of Mn centers compared to Fe ones, a lower OER activity was detected. This trend is in line with literature reports suggesting that a manganese excess may lead to less favorable redox dynamics between the active metal centers, potentially affecting OER kinetics.[25]

4. Conclusions

The present work has reported for the first time on the fabrication of supported MFO electrocatalysts for seawater splitting *via* an original one-pot CVD route, starting from second-generation Mn and Fe precursor mixtures. The latter, acting as single-source precursor thanks to the analogous thermal properties of the two metal complexes, offer a remarkable versatility in controlling the structural and compositional features of the resulting deposits. A comprehensive material characterization by forefront complementary techniques enabled to elucidate the structural, compositional and morphological features of the target systems and highlighted the possibility of directly "transferring" the Mn/Fe ratio from the precursor mixtures to the obtained materials. The latter were characterized by the formation of phase-pure manganese ferrites, with a spinel-type structure and a composition ranging

from $MnFe_2O_4$ to Mn_2FeO_4 upon changing the Mn : Fe precursor molar ratio from 1 : 2 to 2 : 1. The latter modulation resulted in tailored functional performances, favourably promoting oxygen evolution from seawater even at overpotentials lower than the onset of hypochlorite formation, with Tafel slopes between 60 and 70 mV dec^{-1}. These results, favourably positioned in the actual panorama of OER from seawater promoted by various single and mixed-phase oxides/hydroxides, also favorably compare with different benchmark IrO_2 and RuO_2 electrocatalysts. The rationale for the obtained results was grounded on the presence of oxygen vacancies, as well as on Mn/Fe synergistic cooperation directly dependent on their mutual content. Furthermore, the fabricated materials present an appreciable stability and a high selectivity toward O_2 evolution. Taken together, these characteristics render the present electrocatalysts an attractive alternative to expensive noble metal-containing ones for energy production from seawater, a largely available natural resource, preventing detrimental corrosion from Cl-related species.

Basing on the obtained results, various attractive perspectives for future research developments can be foreseen. From a fundamental point of view, *in situ* characterization could be applied to similar growth processes to track precursor decomposition and reaction dynamics and thus enhance material performances. In perspective, complementary computational studies could further contribute to gather a microscopic understanding of the OER process on these complex ferrite systems, and on the origin of selectivity against ClOR. The proposed CVD strategy, offering a precise control over composition and uniformity of the obtained materials, can also be conveniently extended to different substrates to obtain large-area electrodes, for an eventual industrial end-use. A similar application would require an optimization of the catalyst loading, to obtain higher current densities, as well as flow seawater testing to assess resistance to marine impurities and suspended solids. The outcomes of these analyses may also open the door to the use of the developed materials in the production of alternative energy vectors from various natural wastes, to simultaneously attain water purification and energy production.

Author contributions

Alessandro Bigiani: visualization, methodology, data curation, validation, formal analysis, writing – reviewing and editing. Alberto Gasparotto: conceptualization, visualization, methodology, validation, writing – original draft preparation, editing, and funding acquisition. Gian Andrea Rizzi: methodology, validation, investigation, writing – reviewing and editing, and funding acquisition. Cinzia Sada: methodology, data curation, writing – reviewing and editing. Raffaella Signorini: data curation, validation, writing – reviewing and editing. Alessia Famengo: data curation, methodology, writing – reviewing and editing. Davide Barreca: methodology, investigation, supervision and resources, writing – original draft preparation, editing. Oleg I. Lebedev, Evgeny Modin and Mamour Sall: visualization, investigation and data curation. Chiara Maccato: conceptualization, writing – original draft preparation, supervision and resources.

Conflicts of interest

The authors declare that they have no known competing financial interests or personal relationships that could have appeared to influence the work reported in this paper.

Data availability

The data supporting this article are included as part of the supplementary information (SI). Supplementary information: experimental methods: additional results on material synthesis and characterization. See DOI: https://doi.org/10.1039/d5ta10304e.

Acknowledgements

This work was supported by Padova University (PDiSC#02BIRD2023-UNIPD RIGENERA, DOR 2023–2025), INSTM Consortium (TRI.25/013-CIMENTO), and PRIN 2022474YE8 (SCI-TROPHY project; Next Generation EU – Bando PRIN 2022 – M4.C2.1.1). The ESCALAB™ QXi instrumentation was funded by "Sviluppo delle infrastrutture e programma biennale degli interventi del Consiglio Nazionale delle Ricerche" (2019). Thanks are also due to Prof. Gloria Tabacchi and Prof. Ettore Fois (Department of Science and High Technology, Insubria University, Como, Italy) for valuable discussions and support.

References

1 M. Chen, N. Kitiphatpiboon, C. Feng, Q. Zhao, A. Abudula, Y. Ma, K. Yan and G. Guan, *Appl. Catal., B*, 2023, **330**, 122577.
2 T.-Z. Ang, M. Salem, M. Kamarol, H. S. Das, M. A. Nazari and N. Prabaharan, *Energy Strategy Rev.*, 2022, **43**, 100939.
3 T. Cui, X. Zhai, L. Guo, J.-Q. Chi, Y. Zhang, J. Zhu, X. Sun and L. Wang, *Chin. J. Catal.*, 2022, **43**, 2202–2211.
4 M. Ramzan, S. Gouadria, A. G. AlShami and A. Kumar, *Inorg. Chem. Comm.*, 2025, **178**, 114530.
5 M. Umair, M. M. Hassan, B. M. Alotaibi, H. A. Alyousef, A. W. Alrowaily, A. G. Al -Sehemi and K. Tahir, *J. Sol-Gel Sci. Technol.*, 2025, **116**, 1088–1100.
6 A. Zaka, M. Aftab, N. Fatima, K. Mashood, M. A. Asghar, A. Numan, M. S. Ahmad, A. Haider, M. Iqbal, W. A. Shah and M. A. Mansoor, *Fuel*, 2025, **395**, 135179.
7 A. Kumar, B. N. Mahanty, A. Rawat, R. Muhammad, R. K. Panigrahi, D. Pradhan and P. Mohanty, *Energy Fuels*, 2023, **37**, 6810–6823.
8 Y. Zhou, Y. Du, S. Xi and Z. J. Xu, *Electrocatalysis*, 2018, **9**, 287–292.
9 M. M. Mohamed, I. Ibrahim and T. M. Salama, *Appl. Catal., A*, 2016, **524**, 182–191.
10 G. He and Y. Liao, *J. Mater. Chem. A*, 2023, **11**, 6688–6746.
11 M. Benedet, A. Gallo, C. Maccato, G. A. Rizzi, D. Barreca, O. I. Lebedev, E. Modin, R. McGlynn, D. Mariotti and

A. Gasparotto, *ACS Appl. Mater. Interfaces*, 2023, **15**, 47368–47380.
12 S. El Boumlasy, M. Pascale, O. De Luca, T. Caruso, S. Mirabella, A. Terrasi, A. S. Aricò and F. Ruffino, *Appl. Surf. Sci. Adv.*, 2025, **28**, 100809.
13 I. Robina, B. M. Alotaibi, S. Ibrahim, H. A. Alyousef, A. W. Alrowaily, F. N. Almufleh and A. M. Alotaibi, *J. Indian Chem. Soc.*, 2025, **102**, 101817.
14 N. Akechatree, K. Lakshmanan, R. Rajendran, T. Rojviroon, O. Rojviroon and S. Sirivithayapakorn, *J. Water Process Eng.*, 2025, **77**, 108590.
15 M. M. Hossain Bhuiyan and Z. Siddique, *Int. J. Hydrogen Energy*, 2025, **102**, 1026–1044.
16 S. Bishwanathan and P. K. Gupta, *ACS Appl. Energy Mater.*, 2024, **7**, 5467–5478.
17 C. Maccato, L. Bigiani, G. Carraro, A. Gasparotto, R. Seraglia, J. Kim, A. Devi, G. Tabacchi, E. Fois, G. Pace, V. Di Noto and D. Barreca, *Chem.–Eur. J.*, 2017, **23**, 17954–17963.
18 Z. Wang, C. Wang, L. Ye, X. Liu, L. Xin, Y. Yang, L. Wang, W. Hou, Y. Wen and T. Zhan, *Inorg. Chem.*, 2022, **61**, 15256–15265.
19 H. Guermazi, M. Smari, A. Tahir, M. Y. Haik, T. Mnasri, T. u. Haq and Y. Haik, *Int. J. Hydrogen Energy*, 2025, **157**, 150468.
20 S. Dresp, F. Dionigi, M. Klingenhof and P. Strasser, *ACS Energy Lett.*, 2019, **4**, 933–942.
21 E. Beyreuther, S. Grafström, L. M. Eng, C. Thiele and K. Dörr, *Phys. Rev. B: Condens. Matter Mater. Phys.*, 2006, **73**, 155425.
22 S. Barua, A. Balčiūnaitė, D. Upskuvienė, J. Vaičiūnienė, L. Tamašauskaitė-Tamašiūnaitė and E. Norkus, *Coatings*, 2024, **14**, 1074.
23 L. Bigiani, D. Barreca, A. Gasparotto, T. Andreu, J. Verbeeck, C. Sada, E. Modin, O. I. Lebedev, J. R. Morante and C. Maccato, *Appl. Catal., B*, 2021, **284**, 119684.
24 F. Duan, Y. Guo, Y. Huang, G. Ke, T. Han, Y. Zhou and H. He, *Appl. Surf. Sci.*, 2025, **709**, 163795.
25 J. Kim, J. Lee, C. Liu, S. Pandey, S. Woo Joo, N. Son and M. Kang, *Appl. Surf. Sci.*, 2021, **546**, 149124.
26 M. Benedet, G. A. Rizzi, O. I. Lebedev, V. Roddatis, C. Sada, J.-L. Wree, A. Devi, C. Maccato, A. Gasparotto and D. Barreca, *J. Mater. Chem. A*, 2023, **11**, 21595–21609.
27 S. Y. Jung, J. Lee, K. Aydin, J. Jang, C. Ahn, T. Kim, H. Han and Y. K. Jeong, *Appl. Surf. Sci.*, 2024, **649**, 159097.
28 Y. Konno, T. Yamamoto and T. Nagayama, *Nanoscale*, 2021, **13**, 12738–12749.
29 T. Pandiarajan, S. Ravichandran and L. J. Berchmans, *RSC Adv.*, 2014, **4**, 64364–64370.
30 Q. Zhao, Z. Yan, C. Chen and J. Chen, *Chem. Rev.*, 2017, **117**, 10121–10211.
31 K. Yan, Y. Lu and W. Jin, *ACS Sustain. Chem. Eng.*, 2016, **4**, 5398–5403.
32 J. X. Flores-Lasluisa, D. Salinas-Torres, M. V. López-Ramón, C. Moreno-Castilla, M. A. Álvarez, E. Morallón and D. Cazorla-Amorós, *Environ. Res.*, 2022, **204**, 112126.
33 L. Liu, J. Sun, J. Ding, Y. Zhang, T. Sun and J. Jia, *Inorg. Chem.*, 2019, **58**, 13241–13249.
34 R. Nepal, M. Saghayezhian, J. Zhang and R. Jin, *J. Magn. Magn. Mater.*, 2020, **497**, 165955.
35 M. Tang, Y. Zou, Z. Jiang, P. Ma, Z. Zhou, X. Zhu, J. Bao and S.-G. Sun, *J. Energy Chem.*, 2024, **97**, 12–19.
36 P. K. Baruah, N. Mukherjee, B. Bhagat and K. Mukherjee, *Cryst. Growth Des.*, 2024, **24**, 1504–1528.
37 G. Shen, H. Lu and H. Chen, *Catal. Sci. Technol.*, 2024, **14**, 3235–3242.
38 X. Liu, Y.-Q. Huo, L.-K. Yan, N. Fan, K.-Z. Cai and Z.-M. Su, *Chem.–Eur. J.*, 2020, **26**, 14397–14404.
39 A. Gasparotto, C. Maccato, A. Petala, S. Bebelis, C. Sada, D. I. Kondarides and D. Barreca, *ACS Appl. Energy Mater.*, 2019, **2**, 8294–8302.
40 L. Bigiani, M. Hassan, D. Peddis, C. Maccato, G. Varvaro, C. Sada, E. Bontempi, S. Martí-Sánchez, J. Arbiol and D. Barreca, *ACS Appl. Nano Mater.*, 2019, **2**, 1704–1712.
41 D. Barreca, G. Carraro, A. Gasparotto, C. Maccato, C. Sada, A. P. Singh, S. Mathur, A. Mettenbörger, E. Bontempi and L. E. Depero, *Int. J. Hydrogen Energy*, 2013, **38**, 14189–14199.
42 G. Carraro, C. Maccato, E. Bontempi, A. Gasparotto, O. I. Lebedev, S. Turner, L. E. Depero, G. Van Tendeloo and D. Barreca, *Eur. J. Inorg. Chem.*, 2013, **2013**, 5454–5461.
43 G. Carraro, D. Peeters, A. Gasparotto, C. Maccato, E. Bontempi and D. Barreca, *Mater. Lett.*, 2014, **136**, 141–145.
44 D. Barreca, G. Carraro, A. Devi, E. Fois, A. Gasparotto, R. Seraglia, C. Maccato, C. Sada, G. Tabacchi, E. Tondello, A. Venzo and M. Winter, *Dalton Trans.*, 2012, **41**, 149–155.
45 D. Barreca, G. Carraro, A. Gasparotto, C. Maccato, R. Seraglia and G. Tabacchi, *Inorg. Chim. Acta*, 2012, **380**, 161–166.
46 D. Barreca, G. Carraro, E. Fois, A. Gasparotto, F. Gri, R. Seraglia, M. Wilken, A. Venzo, A. Devi, G. Tabacchi and C. Maccato, *J. Phys. Chem. C*, 2018, **122**, 1367–1375.
47 http://imagej.nih.gov/ij/, Accessed September, 2025.
48 Y. Kuang, M. J. Kenney, Y. Meng, W.-H. Hung, Y. Liu, J. E. Huang, R. Prasanna, P. Li, Y. Li, L. Wang, M.-C. Lin, M. D. McGehee, X. Sun and H. Dai, *Proc. Natl. Acad. Sci. U. S. A.*, 2019, **116**, 6624–6629.
49 X. Wang, M. Geng, S. Sun, Q. Xiang, S. Dong, K. Dong, Y. Yao, Y. Wang, Y. Yang, Y. Luo, D. Zheng, Q. Liu, J. Hu, Q. Wu, X. Sun and B. Tang, *J. Mater. Chem. A*, 2024, **12**, 634–656.
50 PDF card no. 73-1964, 2002.
51 S. Tabatabai Yazdi, P. Iranmanesh, S. Saeednia and M. Mehran, *Mater. Sci. Eng.: B*, 2019, **245**, 55–62.
52 K. R. Sanchez-Lievanos, J. L. Stair and K. E. Knowles, *Inorg. Chem.*, 2021, **60**, 4291–4305.
53 M. A. Shilpa Amulya, H. P. Nagaswarupa, M. R. Anil Kumar, C. R. Ravikumar and K. B. Kusuma, *J. Phys. Chem. Solids*, 2021, **148**, 109661.
54 K. Derkaoui, I. Bencherifa, A. Elfiad, Y. Mebdoua, I. Belkhettab, K. Boukhouidem, S. Benredouane, T. Hadjersi, A. Manseri and M. Kechouane, *J. Electron. Mater.*, 2025, **54**, 5271–5286.
55 B. Nandan, M. C. Bhatnagar and S. C. Kashyap, *J. Phys. Chem. Solids*, 2019, **129**, 298–306.
56 K. Vamvakidis, M. Katsikini, D. Sakellari, E. C. Paloura, O. Kalogirou and C. Dendrinou-Samara, *Dalton Trans.*, 2014, **43**, 12754–12765.

57 PDF card no. 80–0382, 2002.
58 PDF card no. 33–0664, 2002.
59 A. R. C. Bredar, M. D. Blanchet, A. R. Burton, B. E. Matthews, S. R. Spurgeon, R. B. Comes and B. H. Farnum, *ACS Catal.*, 2022, **12**, 3577–3588.
60 J. F. Moulder, W. F. Stickle, P. E. Sobol and K. D. Bomben, Physical Electronics Division, Perkin-Elmer Corporation, *Handbook of X-ray Photoelectron Spectroscopy*, 1992.
61 L. Bigiani, C. Maccato, T. Andreu, A. Gasparotto, C. Sada, E. Modin, O. I. Lebedev, J. R. Morante and D. Barreca, *ACS Appl. Nano Mater.*, 2020, **3**, 9889–9898.
62 D. Briggs and M. P. Seah, *Practical Surface Analysis: Auger and X-ray Photoelectron Spectroscopy*, Wiley, New York, 2nd edn, 1990.
63 V. R. Galakhov, M. Demeter, S. Bartkowski, M. Neumann, N. A. Ovechkina, E. Z. Kurmaev, N. I. Lobachevskaya, Y. M. Mukovskii, J. Mitchell and D. L. Ederer, *Phys. Rev. B: Condens. Matter Mater. Phys.*, 2002, **65**, 113102.
64 F. Mattelaer, T. Bosserez, J. Rongé, J. A. Martens, J. Dendooven and C. Detavernier, *RSC Adv.*, 2016, **6**, 98337–98343.
65 Z. Cheng, S. Luo, X. Li, S. Zhang, T. Thang Nguyen, M. Guo and X. Gao, *Appl. Surf. Sci.*, 2021, **566**, 150654.
66 T. Yamashita and P. Hayes, *Appl. Surf. Sci.*, 2008, **254**, 2441–2449.
67 S. Das, S. Pramanik, R. G. Nair and A. Chowdhury, *Surf. Interfaces*, 2024, **54**, 105226.
68 W. Kong, L. Huang, X. Quan and G. L. Puma, *Appl. Catal., B*, 2022, **307**, 121214.
69 L. Akbar, M. Ahmed, I. U. Haq, A. Nawaz and M. S. Bhutta, *Solid State Commun.*, 2024, **378**, 115410.
70 S. Akhtar, A. Hussain, S. Noreen, N. Bibi, M. Bilal Tahir and J. Ur Rehman, *Comput. Theor. Chem.*, 2024, **1235**, 114546.
71 R. F. Pierret, *Semiconductor Fundamentals, Modular Series on Solid State Devices*, Addison-Wesley, 1988, **1**.
72 ICSD card no. 57988.
73 ICSD card no. 125540.
74 H. Tan, J. Verbeeck, A. Abakumov and G. Van Tendeloo, *Ultramicroscopy*, 2012, **116**, 24–33.
75 H. K. Schmid and W. Mader, *Micron*, 2006, **37**, 426–432.
76 C. Maccato, D. Barreca, L. Signorin, E. Scattolin, G. Tabacchi, E. Fois, C. Sada, O. I. Lebedev, A. Gasparotto, E. Modin, E. Pierobon, N. El Habra and G. A. Rizzi, *Catal. Sci. Technol.*, 2025, **15**, 6358–6371.
77 Y. Wu, Y. Yu, W. Shen, Y. Jiang, R. He and M. Li, *J. Colloid Interface Sci.*, 2024, **670**, 132–141.
78 T. Battault, R. Legros and A. Rousset, *J. Eur. Ceram. Soc.*, 1995, **15**, 1141–1147.